Defects and Deformation of Boron Nitride Nanotubes Studied by Joint Nanoscale Mechanical and Infrared Near-Field Microscopy

Xiaoji G. Xu,[†,‡] Leonid Gilburd,[†] Yoshio Bando,[§] Dmitri Golberg,[§] and Gilbert C. Walker*,[†]

[†]Department of Chemistry, University of Toronto, Toronto, Ontario M5S 3H6, Canada
[‡]Department of Chemistry, Lehigh University, 6 E Packer Ave. Bethlehem, Pennsylvania 18015, United States
[§]World Premier International (WPI) Center for Materials Nanoarchitectonics (MANA), National Institute for Materials Science (NIMS), Tsukuba, Ibaraki 305-0044, Japan

ABSTRACT: Boron nitride nanotubes (BNNTs) are a one-dimensional material with high mechanical strength, good electric insulation, exceptional thermal conductivity, and high temperature stability. The presence of defects and deformations in BNNTs at the nanoscale affects their mechanical properties. In this article, we jointly utilize nanomechanical characterization and infrared scattering type near-field microscopy on the same individual BNNTs to study the defects and deformations. A characteristic structural defect of BNNT is revealed by a blue-shift of infrared absorption and discontinuity in adhesion. Polygonal facets have been observed in BNNTs, as supported by their mechanical responses and spectroscopic signatures. The presence of polygonal facets implies one should expect reactive chemical and hyperbolic optical properties of BNNTs.
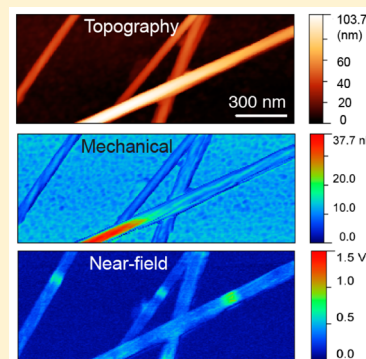
INTRODUCTION

Rich structural information can be obtained by combining mechanical and spectroscopic imaging. Materials with exceptional mechanical properties often contain structural defects that affect their mechanical strength. Vibrational spectroscopies, such as infrared and Raman spectroscopy, have proven useful for the detection of such structural defects.[1−6] However, the spatial resolution of far-field spectroscopies is bound by the optical diffraction limit of the light wavelength, which leads to a spatial resolution of several hundred nanometers for Raman microscopy and of a few micrometers for infrared microscopy. A material with dimensions smaller than the optical diffraction limit often has spatial features such as defects, which cannot be individually resolved by far-field methods, and the correlation between mechanical response and spectroscopic information is difficult to obtain. To bridge this gap and to achieve a simultaneous or sequential mechanical and spectroscopic characterization, a technique with nanoscale resolution is needed.

Boron nitride nanotubes (BNNTs) exhibit exceptional mechanical properties. The mechanical strength and thermal conductivity of BNNTs are comparable to carbon nanotubes.[7−9] In contrast to carbon nanotubes, BNNTs are wide band gap semiconductors, biocompatible,[10] stable at high temperatures, and resistant to oxidization.[11] These properties enable BNNTs as additives to enhance thermal conduction,[12] as useful materials for drug delivery,[13] as strength enhancers in lightweight fabrics[14] and metals,[15−17] and as platforms for deep-UV optical devices.[18,19] A recent discovery has revealed that BNNTs support surface phonon polaritons, which enables nanoscopic confinement and guidance of energy at mid-infrared

frequencies.[20] Various characterization techniques, including high-resolution transmission electron microscopy (HRTEM), electron and X-ray diffraction, atomic force microscopy, and infrared and Raman spectroscopy, have been applied to characterize BNNTs.[8,21,22] Structural defects have been found to be detrimental to mechanical strength and contribute to mechanical failure of the BNNT.[23] Such structural defects can be revealed by HRTEM.[23] However, HRTEM requires a complex, expensive facility and careful sample preparation. The relationship between the TEM images and the optomechanical properties can be largely a matter of speculation, unless the results are obtained under a delicate and time-consuming *in situ* experiment involving nanomanipulation.[24] One would expect defects to disrupt the B−N bonding, which would lead to spectral shifts of local vibrational spectra. However, up until recently, the lack of spatial resolution has prevented vibrational spectroscopies from spatially locating structural defects of BNNTs.[25]

Here we demonstrate sequential mechanical mapping and infrared spectroscopy of BNNTs at ∼15 nm spatial resolution with a scanning probe microscope. Atomic force microscope (AFM) is capable of measurement of adhesion and elasticity at nanoscale.[26−29] In our study, the quantitative nanomechanical mapping is achieved by PeakForce Tapping (also known as peak force tapping).[30] In peak force tapping, the microscope controller dynamically retracts the tip at the peak force amplitude of the tip sample interaction, rather than performing
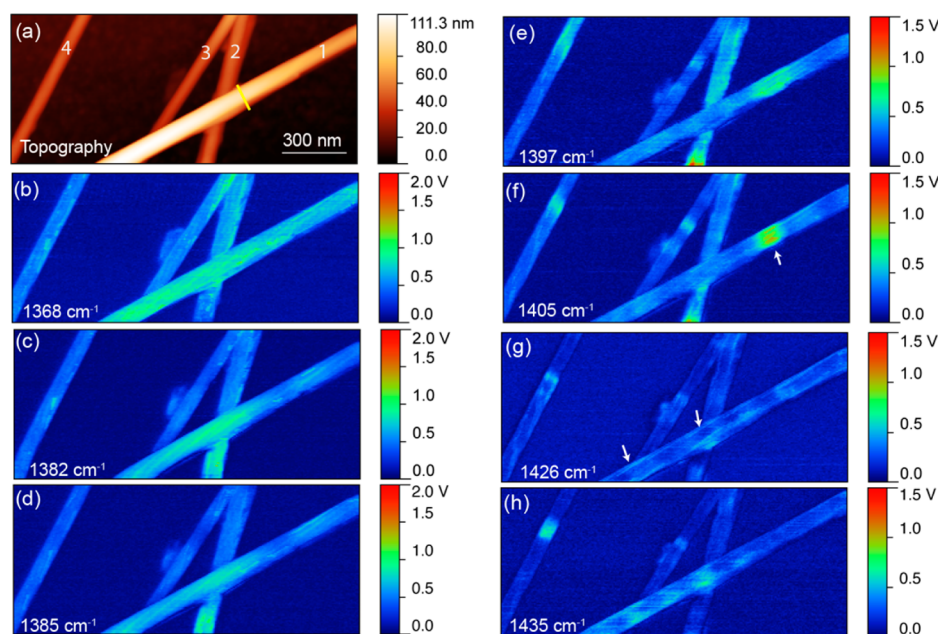
Figure 1. Images of BNNTs. (a) Topography of four BNNTs labeled as 1, 2, 3, and 4, obtained by the tapping mode. (b) Infrared near-field image of the BNNTs at infrared frequency of 1368 cm^{-1}. (c) Near-field images at 1382 cm^{-1}. (d) Near-field images at 1385 cm^{-1}. High intensity ridges are clearly seen at 1382 and 1385 cm^{-1} frequencies. (e) Near-field images at 1397 cm^{-1}. (f) Near-field images at 1405 cm^{-1}. An absorption abnormality is marked with a yellow arrow. (g) Near-field images at 1426 cm^{-1}. (h) Near-field images at 1435 cm^{-1}. Periodical patterns, characteristic of surface phonon polaritons, are observed at 1426 and 1435 cm^{-1}. High near-field filament response is also observed on the near-field image at 1426 cm^{-1}; it is at different locations than in the ridges on (c) and (d).

tip indentation to a fixed distance, as in the case of nanoindentation. Therefore, while obtaining sample mechanical information, the peak force tapping approach avoids hard contact between the tip and the sample, which preserves a sharp and clean tip during imaging. This is a crucial advantage. In scattering type or apertureless near-field microscopy, tip sharpness determines the spatial resolution,[31] and tip cleanness is required for a good signal. Peak force tapping is compatible with scattering type near-field techniques.

Infrared scattering type scanning near-field optical microscopy (s-SNOM) is used for this combined mechanical and infrared spectroscopic study. Specifically, a phase-controlled homodyne technique of s-SNOM is used to achieve chemical sensitive imaging at an ~15 nm spatial resolution. In this technique, a $\pi/2$ phase homodyning approach is utilized to selectively amplify the imaginary part of the near-field signal that corresponds to the infrared absorption.[25] This allows fast near-field chemical sensitive mapping based on the IR absorption of the nanomaterials. Note that other types of near-field techniques, e.g., tip-enhanced Raman spectroscopy (TERS)[32,33] and fiber-based aperture near-field scanning optical microscopy (NSOM),[34] require a high level of probe cleanness. Potential contamination or tip deformation due to probe/sample contact during mechanical measurement would lead to deterioration of TERS or NSOM performance, therefore preventing TERS or fiber-based NSOM from combined operations under mechanical measurement with the same probe.

EXPERIMENTAL METHODS

The core of the apparatus is a stage-scanning atomic force microscope (Multimode 8 AFM, Bruker Nano). The AFM operates in the tapping mode for s-SNOM and PeakForce Tapping mode for nanomechanical mapping. A custom optical setup built to perform s-SNOM was described previously.[25,35] In the s-SNOM setup, a quantum cascade laser (QCL Daylight Solutions) is used to provide a frequency tunable infrared laser to match the phonon resonance and surface phonon polariton (SPhP) resonance of the BNNTs. The infrared laser is focused by a parabolic mirror of N.A. 0.24 to the tip apex of a metal-coated AFM probe tip (DPE-14 Mikromash), which oscillates at 140 kHz with a 30 nm oscillation amplitude. The scattered light is collected and interferometrically homodyned with a reference laser field from the same source. The optical path difference of the two interferometer arms is stabilized with a feedback loop to maintain a phase difference of $\pi/2$. An infrared detector (JD1512, Teledyne-Judson) is used to convert the homodyned infrared light to a voltage signal, which is demodulated by a lock-in amplifier (HF2Li, Zurich Instrument) at the third harmonic of the AFM tip tapping frequency. Collection of one s-SNOM image based on near-field absorption with 256 by 256 pixels takes approximately 3 min. Near-field images are collected at different infrared frequencies across the phonon resonances of the BNNTs.

The peak force tapping imaging capability is achieved with an AFM controller (Nanoscope V, Bruker).[30] The sample stage is oscillated at 1 kHz frequency. The deflection of the AFM cantilever is monitored. The stage oscillation amplitude is dynamically adjusted to maintain a maximal peak force deflection at the closest point of contact. Unlike tapping mode (intermittent contact mode) imaging, the motion of the cantilever is not nearly resonant. The cantilever deflection vs stage position curves are recorded when the sample is periodically approaching the tip and retracting from the tip. The elasticity is calculated from the slope of the approaching and retracting curves with the controlling software based on the Derjaguin−Muller−Toporov (DMT) model.[36] The adhesion is calculated from the difference in areas under the approaching

and retracting curves. A calibration procedure is used to calibrate the parameters of the cantilever with a calibration sample of known elasticity. In this case, the gold substrate is used as the calibration sample, which has a Young's modulus of 80 GPa. One image of 256 by 256 pixels takes about 5 min to acquire. The peak force tapping measurements are carried out on the same sample area right after the infrared near-field measurements; i.e., the data are sequentially, not simultaneously, obtained. The parameters of the peak force measurement are chosen to let the modulus read out from the reference substrate (in our case, a gold substrate) to match the literature value: this accounts for the systematic error of the tip shape and force calibration. A deterioration of the AFM probe tip is not observed, as the s-SNOM images before and after peak force tapping give virtually the same near-field images.

The multiwall BNNTs were synthesized using a high temperature chemical vapor deposition (CVD) synthesis method as described in the literature.[37] The BNNTs were dispersed in isopropanol under sonication for a few hours and drop-cast on flat gold substrates of root-mean-square roughness of ~1.7 nm.

■ RESULTS

Infrared Near-Field Microscopy. A representative area with four BNNTs (labeled as 1, 2, 3, and 4) is chosen for the joint spectroscopic and nanomechanical study. Figure 1a shows the AFM topography of the sample revealed undertraditional tapping mode, coregistered during the IR s-SNOM measurement. The AFM topography image shows the shape of the nanotubes; spectroscopic and mechanical information from these nanotubes are not obtained. Figure 1b−h depicts the infrared near-field images obtained with the $\pi/2$ phase-controlled homodyne technique. Under the $\pi/2$ homodyne condition, the imaginary part of the near-field signal is measured, which corresponds to near-field absorption from BN local phonon resonances and surface phonon polariton resonances. As the infrared laser frequency is increased, a progression of BNNT near-field responses is observed—these are due to both the BN local phonon and propagating surface phonon polariton responses.[20,25] Collected at the infrared frequency of 1368 cm^{-1}, the near-field image shown in Figure 1b displays homogeneous near-field responses across all four nanotubes, reflecting local phonon absorption. Starting at the infrared frequency of 1382 cm^{-1}, tube 1 shows few features, including the development of periodical nodal patterns in the signal, characteristic of propagating waves of surface phonon polaritons. The periodicity shrinks with the increase of infrared probe frequencies. Such observations of local phonon and surface phonon polaritons have been reported by us previously,[20,25] and for brevity they are not extensively discussed here. However, a novel feature is observed. At 1382 and 1385 cm^{-1} infrared frequencies, the near-field images in Figures 1c and 1d reveal twisting, high intensity, mutual parallel ridges along nanotube 1, with an angle of 8° from the direction of the long axis of the nanotube. Such twisted edges are not observed on the AFM topography or near-field images at higher infrared frequencies. In addition, a localized strong increase of the near-field absorption is observed at 1408 cm^{-1} (marked by the yellow arrow in Figure 1f), which could be related to structural defects. However, other types of joint characterization tools, preferably nanomechanical measurements, are required to validate such a correlation.

Quantitative Nanomechanical Mapping. Quantitative nanomechanical maps of these four BNNTs are obtained after the infrared s-SNOM measurement. Figure 2a shows the AFM
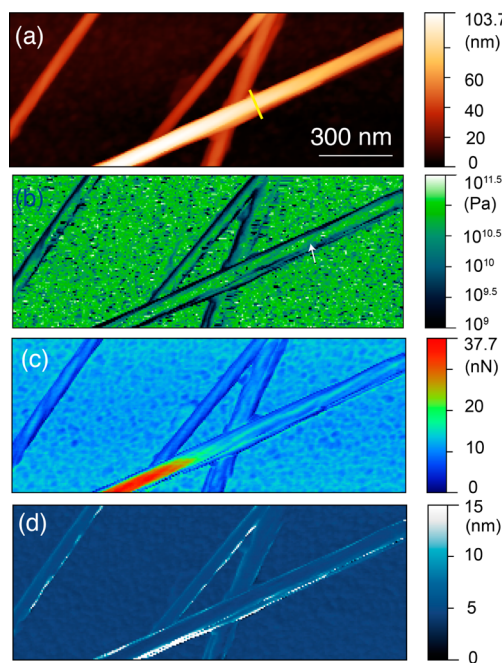

Figure 2. Quantitative nanomechanical mapping of BNNTs. (a) Topography of the same BNNTs obtained in the peak force tapping mode. (b) Apparent modulus map of the BNNTs. Twisting strands are identifiable. (c) Adhesion map of the BNNTs. Twisting strands are identifiable. (d) Deformation map of the peak force tapping measurement.

topography from peak force tapping. It is worth noting that, in comparison to data from traditional tapping mode, the topography from peak force tapping gives higher spatial resolution with the same probe due to a closer tip interaction with the sample. Other than this, the topography from peak force tapping shows nearly the same shape of these BNNTs on the smooth gold substrate. Figure 2b shows the radial modulus obtained from the peak force tapping image. The BNNT exhibits a local radial modulus on the order of tens of GPa up to 200 GPa. There are noticeable radial modulus variations along BNNTs. The average radial modulus of tube 1 is 65 ± 32 GPa. At the location marked by the white arrow, the modulus is 51 ± 17 GPa. This location corresponds to abnormal near-field absorption at 1405 cm^{-1} observed in the near-field measurement of Figure 1f. The average radial modulus of tube 4 is 45 ± 32 GPa. The radial modulus is much lower than the bending modulus obtained in the three-point nanodeformation measurements[24,38] due to the fact that the radial modulus measurement is done locally with small deformation. The relatively large standard deviation is due to the error on real-time fitting of the approach and retract force−distance curves: the measurement errors are propagated in the machine extraction. As a reference, the gold substrate gives consistently standard deviation of ~40 GPa at five different areas (the standard deviation of the mean from five measurements is consequently 18 GPa). From the modulus image, there are spatially discernible substructures within BNNTs 1 and 4, which appear to be twisted strands in a helical pattern. Figure 2c shows an adhesion map of the BNNTs. There are obvious

twisting substrands in tube 1 as well as in tube 4, based on the adhesion map. The angles between a strand and the direction of the nanotube are found to be 8° for tube 1 and 9° for tube 4. At the same location of the BNNT, the twisting strands from tube 1 show a similar angle to the twisting edges from the near-field images of Figures 1c and 1d. The deformation map from peak force tapping is shown in Figure 2d. The deformations of all four BNNTs are on average ca. 4.5 nm. The high deformation read-out at the edge of the BNNTs is observed possibly due to the abrupt topographic changes and reduced tip–sample contact area when the probe is passing over the edge and, consequently, a large discrepancy between approach curves and retract curves in peak force tapping analysis.

■ ANALYSIS AND DISCUSSION

Correlating the near-field measurements with the nano-mechanical measurements not only adds confidence in the interpretation of one property map but also enables new findings that cannot be obtained by the measurement of one property alone.

Polygonal Shape of BNNT. Both the infrared near-field and peak force tapping images indicate that for a large diameter BNNT (tube 4, with diameter of ∼70 nm) the outer tubes are polygonal rather than circular cylinders. This observation agrees with previous reports based on TEM[23] and electron diffraction,[39] which suggest that large diameter multiwall BNNTs undergo polygonization, i.e., layers form polygons instead of cylinders in a cross section natural for small diameter tubes. Such polygonization indicates that a polygon with a large area of h-BN crystalline surface has a lower configuration energy than that of a circular tube. h-BN allows planar sp^2 orbital hybridization, which results in lower energy. On the other hand, a tubular shape requires the h-BN plane to have curvature, which means an increase of configuration energy from the planar structures. For BNNTs of a large outer diameter, polygonization allows a reduction of configuration energies for most of the in-plane BN bonds, at the expense of likely higher energy BN bonding at the edge where two planes meet. As the diameter increases, the percentage of boron and nitrogen atoms at the edges decreases, and the average bond energy approaches that of h-BN. A stacked planar outer layer also allows organized and compact interplane Coulomb interactions,[40] which further reduces the net configuration energy. In addition, from both near-field imaging and nanomechanical mapping, it is found that the polygon of the nanotubes exhibits twists along the direction of the BNNT with an angle of ∼8°. This angle is perhaps coincidentally, within the range of typical chirality of multiwall BNNTs.[41]

The presence of polygonal BN surfaces is reflected by the nanomechanical responses. Figure 3a shows the overlay of modulus, adhesion, and topography, across a profile that is marked by a yellow line in Figure 2a. A polygonal shape (dashed shape) can be estimated from the peak force tapping topography. The topography shows a tilted flat top of a possible hexagon. The apparent modulus is higher at the edges than at the middle of the polygonal plane. On the other hand, adhesion is higher at the middle of the plane than at its edges. This is understandable, considering that the polygonal plane provides a larger contact area therefore stronger attractive interaction forces between the plane and the tip than between the tip and the edges. In addition, the presence of polygonal shapes in BNNT also explains the higher radial modulus observed, in comparison to circular-shaped BNNTs. The radial modulus
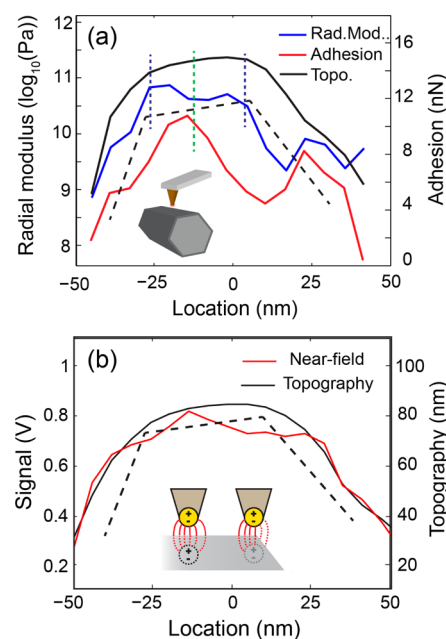

Figure 3. Mechanical and near-field response profiles across a polygonal cross section. (a) Overlap of apparent modulus, adhesion, and topography of a BNNT profile obtained from peak force tapping mode along a profile marked by a yellow line in Figure 2a. The polygonal plane is identifiable from the topography and is shown schematically with dashed lines. The apparent modulus reveals an increase at the edge of the planes and a decrease the middle of the plane. As a comparison, the middle of the plane exhibits higher adhesion than the edge. The inset displays a scheme of an AFM tip and a polygonal BNNT. (b) Overlap of near-field images and topography of a profile of a BNNT, marked by a yellow line in Figure 1a. The near-field profile is taken at 1382 cm^{-1}. It shows an increase of near-field signal at the middle of the polygonal plane. Such an increase of infrared absorption signal in the polygonal plane is likely due to strong image dipole (see inset) and higher crystallinity of BN at the plane.

values from the measured polygonal BNNTs shown in Figure 2 are higher than the predicted literature value of 24 GPa of radial modulus for circular BNNTs of similar diameter.[42]

The infrared near-field response at the transverse optical BN phonon frequency also reflects the polygonization of the BNNTs. Figure 3b illustrates the overlay of near-field responses of 1382 cm^{-1} with tapping mode topography along the same profile of Figure 3a, marked by a yellow line in Figure 1a. The polygonal shape (dashed shape) can be estimated by the tapping mode topography. It can be discerned that the near-field responses from the middle of the polygonal plane is higher than that from the edges. This phenomenon has two possible interpretations: (i) the planar surface at the middle of the polygon generates more efficient image dipoles of the tip than those from the edge of the polygon (see inset of Figure 3b) or (ii) the middle of the plane has a better organized crystalline structure than at the edge of the BNNT; the better organized crystalline structures lead to stronger infrared absorption at the phonon resonance. The first interpretation is related to the signal generation scheme of s-SNOM.[43] The second interpretation is necessary to explain the presence of the twisting ridges at the BN phonon frequencies (1360−1385 cm^{-1}) that are not observed at SPhP frequencies (>1385 cm^{-1}). With the second interpretation, one would expect an
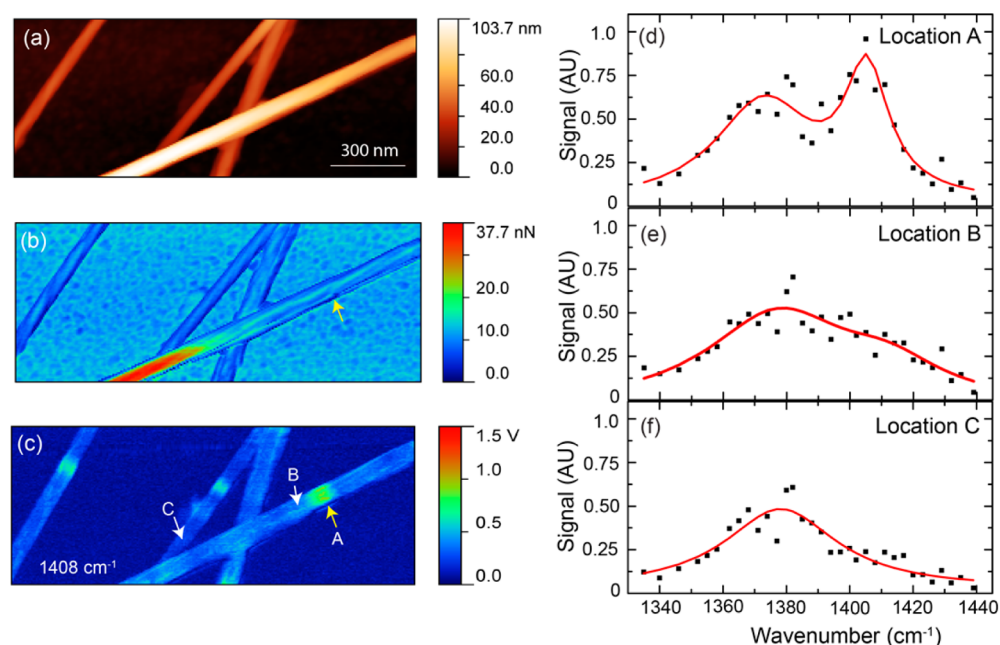
Figure 4. Correlative study of a structural defect. (a) Topography of the BNNTs. (b) Adhesion to the BNNTs by AFM tip. The arrow marks a structural defect that corresponds to a discontinuity of adhesion response from the nanomechanical measurement. (c) The near-field image taken at 1408 cm^{-1} shows a localized increase of infrared response at the structural defect location, marked by A. (d−f) Infrared spectra at locations A, B, and C, marked in (c). The structural defect corresponds to an emergence of narrow line width absorption at 1405 cm^{-1}. In contrast, immediate adjacent location B lacks such responses, nor does location C.

overall increase of near-field signals at all resonant frequencies from the first interpretation alone.

Correlative Mechanical and Spectroscopic Defect Detection. The combination of nanomechanical and near-field infrared capability enables effective identification of the structural defects of BNNTs. Figure 4a−c shows the topography, adhesion, and near-field images, respectively, of a BNNT defect (marked by a yellow arrow). While the topography provides limited indication of the location of the defect, both adhesion and near-field images display clear response abnormality. At the defect location, the adhesion map exhibits a discontinuity of the BN polygon plane, and the near-field image at 1408 cm^{-1} reveals an enhanced near-field absorption. The infrared spectrum is assembled by extracting multiple near-field responses across the BN phonon and SPhP resonances. Figure 4d illustrates the infrared spectrum obtained at the defect location, labeled as location A in Figure 4c. The spectrum of an adjacent location, labeled as location B, and the spectrum of a BNNT at location C are presented in Figures 4e and 4f as references. All three locations show a phonon resonance around 1375 cm^{-1}. The phonon resonance at location A is 1372 cm^{-1} with line width of 37 cm^{-1}; location B is resonant at 1377 cm^{-1} with a line width of 54 cm^{-1}; location C is resonant at 1378 cm^{-1} with a line width of 43 cm^{-1}. The defect at location A is associated with a strong absorption within the SPhP resonance frequency, centered at 1405 cm^{-1} with a line width of 16 cm^{-1}. As a comparison, despite a separation of only ∼100 nm, adjacent location B has only a very weak near-field absorption at 1412 cm^{-1}. Location C does not resonate at this frequency. The main near-field infrared absorption below 1380 cm^{-1} is present at all locations and corresponds to the BN transverse optical phonon resonance. The high frequency resonance centered around 1405 cm^{-1} and higher can be attributed to the presence of less organized turbostratic BN (t-BN),[44,45] in comparison to well-organized *h*-

BN. A defect of t-BN leads to large disturbance of a B−N bond that leads to a blue-shift of the phonon absorption. The modification of BN bonds by a defect is local, within a short range, as indicated by the near-field imaging of Figures 1f and 4c. Other possible explanations of the blue-shift of infrared spectra, such as that a defect serves as a scattering center for propagating surface phonon polaritons, are also possible but unlikely since at some SPhP frequencies, SPhP scattering at the defect site is not seen.

Implications of Polygonal Shape of BNNT for Nano-Optical Applications. From the perspective of BNNT as an optical material, the presence of twisting infrared absorbing polygonal planes indicates that such polygonal BNNTs may possess birefringence at the mid-infrared frequencies. Moreover, *h*-BN is found to be a hyperbolic material[46] that has special nanophotonic properties for wave guiding and field concentration.[47,48] Polygonal BNNTs contain planes of *h*-BN that are hyperbolic materials. This enables the use of polygonal BNNTs as a novel nanophotonic material.

The continuous distribution of surface phonon polaritons in the polygonal BNNTs at 1426 and 1435 cm^{-1}, as shown in Figures 1g and 1h, means that the presence of the polygonal planes does not affect the travel of the SPhPs along the BNNT. This can be understood by the fact that SPhPs are a hybrid between lattice vibrations and the bound electromagnetic field. Adjacent polygonal BN planes share the same electromagnetic near field of SPhP that efficiently transfers polariton energy, and as long as the edges between two BN polygonal planes are not dissipative, the SPhP will persist along the BNNT. Moreover, at the SPhP active frequency, the edges of the polygonal planes exhibit higher near-field signal, indicating further field concentration of SPhP waves at the sharp edges in addition to the field enhancement due to the presence of SPhP (marked by white arrows in Figure 1g). This finding is made

possible by the combined infrared near-field and nanomechanical measurements.

The polygonization of large diameter BNNTs also means different chemical properties. For perfectly circular BNNT or planar h-BN, boron and nitrogen atoms form sp^2 hybrids. For polygonal BNNT, at the edges, boron and nitrogen atoms have not purely sp^2 orbital hybridization. High-energy states of BN and low band gap at the edges are possible, which means potentially higher chemical and photochemical reactivity. Edges also provide an opportunity for enhanced generation of desired molecules, and species, which might be photoactive, and the near-field technique can be used as a probe to investigate such chemical reactions at the edges. It worth noting that the polygonal cross-section of BNNTs may be rationally designed by the synthesis method, which will require additional investigation.

■ SUMMARY

The joint multimodal characterization with infrared spectroscopic and nanomechanical imaging enables correlative investigations on inhomogeneous nanomaterials with tens of nanometers spatial resolution. With such capabilities, we have correlated the infrared signatures and mechanical responses of the structural defects from individual boron nitride nanotubes. In addition, large diameter BNNTs are found to be polygonal, which provides for future opportunities to design mechanical, chemically reactive, infrared field concentration, and hyperbolic optical properties based on BNNTs.

■ AUTHOR INFORMATION

Corresponding Author
*E-mail: gwalker@chem.utoronto.ca (G.C.W.).

Notes
The authors declare no competing financial interest.

■ ACKNOWLEDGMENTS

■ REFERENCES

(1) Johnson, N.; Ponce, F.; Street, R.; Nemanich, R. Defects in Single-Crystal Silicon Induced by Hydrogenation. *Phys. Rev. B: Condens. Matter Mater. Phys.* **1987**, *35*, 4166−4169.

(2) Hollins, P. The Influence of Surface Defects on the Infrared Spectra of Adsorbed Species. *Surf. Sci. Rep.* **1992**, *16*, 51−94.

(3) McNamara, K.; Williams, B.; Gleason, K.; Scruggs, B. Identification of Defects and Impurities in Chemical-Vapor-Deposited Diamond through Infrared Spectroscopy. *J. Appl. Phys.* **1994**, *76*, 2466−2472.

(4) Lebedeva, N.; Rodes, A.; Feliu, J.; Koper, M.; Van Santen, R. Role of Crystalline Defects in Electrocatalysis: Co Adsorption and Oxidation on Stepped Platinum Electrodes as Studied by in Situ Infrared Spectroscopy. *J. Phys. Chem. B* **2002**, *106*, 9863−9872.

(5) Nakashima, S.; Nakatake, Y.; Ishida, Y.; Talkahashi, T.; Okumura, H. Detection of Defects in Sic Crystalline Films by Raman Scattering. *Physica B* **2001**, *308*, 684−686.

(6) Theodorakopoulos, N.; Jäckle, J. Low-Frequency Raman Scattering by Defects in Glasses. *Phys. Rev. B* **1976**, *14*, 2637−2641.

(7) Chopra, N. G.; Luyken, R.; Cherrey, K.; Crespi, V. H.; Cohen, M. L.; Louie, S. G.; Zettl, A. Boron Nitride Nanotubes. *Science* **1995**, *269*, 966−967.

(8) Golberg, D.; Bando, Y.; Tang, C.; Zhi, C. Boron Nitride Nanotubes. *Adv. Mater.* **2007**, *19*, 2413−2432.

(9) Tang, C.; Bando, Y.; Liu, C.; Fan, S.; Zhang, J.; Ding, X.; Golberg, D. Thermal Conductivity of Nanostructured Boron Nitride Materials. *J. Phys. Chem. B* **2006**, *110*, 10354−10357.

(10) Ciofani, G.; Danti, S.; Genchi, G. G.; Mazzolai, B.; Mattoli, V. Boron Nitride Nanotubes: Biocompatibility and Potential Spill-over in Nanomedicine. *Small* **2013**, *9*, 1672−1685.

(11) Chen, Y.; Zou, J.; Campbell, S. J.; Le Caer, G. Boron Nitride Nanotubes: Pronounced Resistance to Oxidation. *Appl. Phys. Lett.* **2004**, *84*, 2430−2432.

(12) Zhi, C.; Bando, Y.; Terao, T.; Tang, C.; Kuwahara, H.; Golberg, D. Towards Thermoconductive, Electrically Insulating Polymeric Composites with Boron Nitride Nanotubes as Fillers. *Adv. Funct. Mater.* **2009**, *19*, 1857−1862.

(13) Ciofani, G.; Raffa, V.; Yu, J.; Chen, Y.; Obata, Y.; Takeoka, S.; Menciassi, A.; Cuschieri, A. Boron Nitride Nanotubes: A Novel Vector for Targeted Magnetic Drug Delivery. *Curr. Nanosci.* **2009**, *5*, 33−38.

(14) Smith, M. W.; Jordan, K. C.; Park, C.; Kim, J.-W.; Lillehei, P. T.; Crooks, R.; Harrison, J. S. Very Long Single-and Few-Walled Boron Nitride Nanotubes Via the Pressurized Vapor/Condenser Method. *Nanotechnology* **2009**, *20*, 505604.

(15) Yamaguchi, M.; Meng, F.; Firestein, K.; Tsuchiya, K.; Golberg, D. Powder Metallurgy Routes toward Aluminum Boron Nitride Nanotube Composites, Their Morphologies, Structures and Mechanical Properties. *Mater. Sci. Eng., A* **2014**, *604*, 9−17.

(16) Yamaguchi, M.; Tang, D.-M.; Zhi, C.; Bando, Y.; Shtansky, D.; Golberg, D. Synthesis, Structural Analysis and in Situ Transmission Electron Microscopy Mechanical Tests on Individual Aluminum Matrix/Boron Nitride Nanotube Nanohybrids. *Acta Mater.* **2012**, *60*, 6213−6222.

(17) Yamaguchi, M.; Pakdel, A.; Zhi, C.; Bando, Y.; Tang, D.-M.; Faerstein, K.; Shtansky, D.; Golberg, D. Utilization of Multiwalled Boron Nitride Nanotubes for the Reinforcement of Lightweight Aluminum Ribbons. *Nanoscale Res. Lett.* **2013**, *8*, 1−6.

(18) Li, L. H.; Chen, Y.; Lin, M.-Y.; Glushenkov, A. M.; Cheng, B.-M.; Yu, J. Single Deep Ultraviolet Light Emission from Boron Nitride Nanotube Film. *Appl. Phys. Lett.* **2010**, *97*, 141104.

(19) Jaffrennou, P.; Barjon, J.; Lauret, J. S.; Maguer, A.; Golberg, D.; Attal-Trétout, B.; Ducastelle, F.; Loiseau, A. Optical Properties of Multiwall Boron Nitride Nanotubes. *Phys. Status Solidi B* **2007**, *244*, 4147−4151.

(20) Xu, X. G.; Ghamsari, B. G.; Jiang, J.-H.; Gilburd, L.; Andreev, G. O.; Zhi, C.; Bando, Y.; Golberg, D.; Berini, P.; Walker, G. C. One-Dimensional Surface Phonon Polaritons in Boron Nitride Nanotubes. *Nat. Commun.* **2014**, *5*, 4782.

(21) Arenal, R.; Ferrari, A.; Reich, S.; Wirtz, L.; Mevellec, J.-Y.; Lefrant, S.; Rubio, A.; Loiseau, A. Raman Spectroscopy of Single-Wall Boron Nitride Nanotubes. *Nano Lett.* **2006**, *6*, 1812−1816.

(22) Zhi, C.; Bando, Y.; Tang, C.; Golberg, D.; Xie, R.; Sekigushi, T. Phonon Characteristics and Cathodolumininescence of Boron Nitride Nanotubes. *Appl. Phys. Lett.* **2005**, *86*, 213110.

(23) Golberg, D.; Costa, P. M. F. J.; Lourie, O.; Mitome, M.; Bai, X.; Kurashima, K.; Zhi, C.; Tang, C.; Bando, Y. Direct Force Measurements and Kinking under Elastic Deformation of Individual Multiwalled Boron Nitride Nanotubes. *Nano Lett.* **2007**, *7*, 2146−2151.

(24) Wei, X.; Wang, M. S.; Bando, Y.; Golberg, D. Tensile Tests on Individual Multi-Walled Boron Nitride Nanotubes. *Adv. Mater.* **2010**, *22*, 4895−4899.

(25) Xu, X. G.; Tanur, A. E.; Walker, G. C. Phase Controlled Homodyne Infrared near-Field Microscopy and Spectroscopy Reveal Inhomogeneity within and among Individual Boron Nitride Nanotubes. *J. Phys. Chem. A* **2013**, *117*, 3348−3354.

(26) Radmacher, M.; Fritz, M.; Cleveland, J. P.; Walters, D. A.; Hansma, P. K. Imaging Adhesion Forces and Elasticity of Lysozyme Adsorbed on Mica with the Atomic Force Microscope. *Langmuir* **1994**, *10*, 3809−3814.

(27) Chen, Q.; Schönherr, H.; Vancso, G. J. Mechanical Properties of Block Copolymer Vesicle Membranes by Atomic Force Microscopy. *Soft Matter* **2009**, *5*, 4944−4950.

(28) Xu, C.; Jones, R. L.; Batteas, J. D. Dynamic Variations in Adhesion of Self-Assembled Monolayers on Nanoasperities Probed by Atomic Force Microscopy. *Scanning* **2008**, *30*, 106−117.

(29) Schön, P.; Bagdi, K.; Molnár, K.; Markus, P.; Pukánszky, B.; Vancso, G. J. Quantitative Mapping of Elastic Moduli at the Nanoscale in Phase Separated Polyurethanes by Afm. *Eur. Polym. J.* **2011**, *47*, 692−698.

(30) Pettenger, B.; Erina, N.; Su, C. Quantitative Mechanical Property Mapping at the Nanoscale with Peakforce Qnm. *Bruker Application Note* **2010**, 128.

(31) Novotny, L.; Stranick, S. J. Near-Field Optical Microscopy and Spectroscopy with Pointed Probes. *Annu. Rev. Phys. Chem.* **2006**, *57*, 303−331.

(32) Hayazawa, N.; Inouye, Y.; Sekkat, Z.; Kawata, S. Near-Field Raman Scattering Enhanced by a Metallized Tip. *Chem. Phys. Lett.* **2001**, *335*, 369−374.

(33) Stöckle, R. M.; Suh, Y. D.; Deckert, V.; Zenobi, R. Nanoscale Chemical Analysis by Tip-Enhanced Raman Spectroscopy. *Chem. Phys. Lett.* **2000**, *318*, 131−136.

(34) Dürig, U.; Pohl, D.; Rohner, F. Near-Field Optical-Scanning Microscopy. *J. Appl. Phys.* **1986**, *59*, 3318−3327.

(35) Xu, X. G.; Gilburd, L.; Walker, G. C. Phase Stabilized Homodyne of Infrared Scattering Type Scanning near-Field Optical Microscopy. *Appl. Phys. Lett.* **2014**, *105*, 263104.

(36) Derjaguin, B. V.; Muller, V. M.; Toporov, Y. P. Effect of Contact Deformations on the Adhesion of Particles. *J. Colloid Interface Sci.* **1975**, *53*, 314−326.

(37) Zhi, C.; Bando, Y.; Tan, C.; Golberg, D. Effective Precursor for High Yield Synthesis of Pure Bn Nanotubes. *Solid State Commun.* **2005**, *135*, 67−70.

(38) Tanur, A. E.; Wang, J.; Reddy, A. L.; Lamont, D. N.; Yap, Y. K.; Walker, G. C. Diameter-Dependent Bending Modulus of Individual Multiwall Boron Nitride Nanotubes. *J. Phys. Chem. B* **2013**, *117*, 4618−4625.

(39) Golberg, D.; Mitome, M.; Bando, Y.; Tang, C.; Zhi, C. Multi-Walled Boron Nitride Nanotubes Composed of Diverse Cross-Section and Helix Type Shells. *Appl. Phys. A: Mater. Sci. Process.* **2007**, *88*, 347−352.

(40) Garel, J.; Leven, I.; Zhi, C.; Nagapriya, K.; Popovitz-Biro, R.; Golberg, D.; Bando, Y.; Hod, O.; Joselevich, E. Ultrahigh Torsional Stiffness and Strength of Boron Nitride Nanotubes. *Nano Lett.* **2012**, *12*, 6347−6352.

(41) Celik-Aktas, A.; Zuo, J.-M.; Stubbins, J. F.; Tang, C.; Bando, Y. Double-Helix Structure in Multiwall Boron Nitride Nanotubes. *Acta Crystallogr., Sect. A: Found. Crystallogr.* **2005**, *61*, 533−541.

(42) Chiu, H.-C.; Kim, S.; Klinke, C.; Riedo, E. Morphology Dependence of Radial Elasticity in Multiwalled Boron Nitride Nanotubes. *Appl. Phys. Lett.* **2012**, *101*, 103109.

(43) Knoll, B.; Keilmann, F. Enhanced Dielectric Contrast in Scattering-Type Scanning near-Field Optical Microscopy. *Opt. Commun.* **2000**, *182*, 321−328.

(44) Thomas, J.; Weston, N. E.; O'Connor, T. E. Turbostratic Boron Nitride, Thermal Transformation to Ordered-Layer-Lattice Boron Nitride. *J. Am. Chem. Soc.* **1962**, *84*, 4619−4622.

(45) Lian, G.; Zhang, X.; Tan, M.; Zhang, S.; Cui, D.; Wang, Q. Low-Temperature Solid State Synthesis and in Situ Phase Transformation to Prepare Nearly Pure Cbn. *Dalton Trans.* **2011**, *40*, 6961−6967.

(46) Poddubny, A.; Iorsh, I.; Belov, P.; Kivshar, Y. Hyperbolic Metamaterials. *Nat. Photonics* **2013**, *7*, 948−957.

(47) Dai, S.; Fei, Z.; Ma, Q.; Rodin, A. S.; Wagner, M.; McLeod, A. S.; Liu, M. K.; Gannett, W.; Regan, W.; Watanabe, K.; et al. Tunable Phonon Polaritons in Atomically Thin Van Der Waals Crystals of Boron Nitride. *Science* **2014**, *343*, 1125−1129.

(48) Woessner, A.; Lundeberg, M. B.; Gao, Y.; Principi, A.; Alonso-González, P.; Carrega, M.; Watanabe, K.; Taniguchi, T.; Vignale, G.; Polini, M.; et al. Highly Confined Low-Loss Plasmons in Graphene−Boron Nitride Heterostructures. *Nat. Mater.* **2015**, *14*, 421−425.